

1 INTRODUCTION

2 Above Earth's atmosphere are the a pair of Van Allen radiation belts, a complex
3 and dynamic plasma environment that affects our technology-driven society. These
4 effects include: a higher radiation dose for astronauts and cosmonauts, higher chance
5 of spacecraft failure due to single event upsets that can lead to catastrophic latchups,
6 degradation of silicon (changing the silicon doping) from an extended radiation dose
7 that can degrade a transistor to the point where it no longer function as a switch,
8 and the degradation of the ozone layer due to the chemical production of NO_X and
9 HO_X molecules. With these effects in mind, it is no surprise that the radiation belts
10 have been extensively studied since their discovery in the 1960s.

11 One natural phenomenon in the radiation belts that has been a topic of interest
12 in the space physics community is wave-particle interactions that, as we will explore
13 throughout this dissertation, can accelerate particles to very high energies (e.g. \approx
14 MeV for electrons) and scatter them into the atmosphere.

15 The goal of this dissertation is to study the wave-particle scattering mechanism
16 that scatters electron microbursts. Electron microbursts, henceforth referred to
17 as microbursts, are typically observed by low Earth orbiting spacecraft, sounding
18 rockets, and high altitude balloons as a sub-second impulse of electrons. Some of
19 the most intense microbursts are observed as a 10 to 100 fold increase of electrons
20 (for example see Fig. 7 in Blake et al. (1996)). Since they were first reported by
21 Anderson and Milton (1964), the short microburst duration and their impulsive nature
22 have compelled countless researchers to understand their properties and the physical
23 mechanism(s) that create microbursts. Microbursts are widely believed to be created
24 by wave-particle scattering between a plasma wave called whistler mode chorus
25 and outer radiation belt electrons, although many details regarding the scattering

²⁶ mechanism are unconstrained or unknown.

²⁷ This chapter serves as an introduction to the physics of charged particles, plasma
²⁸ waves, and the wave-particle interactions in Earth's magnetosphere. We will first
²⁹ derive the motion of individual charged particles in Earth's electric and magnetic
³⁰ fields. Then we will cover how various groups of charged particles coalesce to form
³¹ the major particle populations in the magnetosphere. Then, we will cover the various
³² mechanisms that accelerate particles in the magnetosphere. Lastly, we will review
³³ the basics of microbursts as a jumping-off point for the rest of the dissertation.

³⁴ Charged Particle Motion in Electric and Magnetic Fields

A charged particle trapped in the magnetosphere will experience three types of periodic motion in Earth's nearly dipolar magnetic field. The three motions are ultimately due to the Lorentz force that a particle of momentum \vec{p} , charge q , and velocity \vec{v} experiences in an electric field \vec{E} and magnetic field \vec{B} and is given by

$$\frac{d\vec{p}}{dt} = q(\vec{E} + \vec{v} \times \vec{B}). \quad (1.1)$$

³⁵ In the magnetosphere, the three periodic motions, in decreasing frequency, are
³⁶ gyration, bounce, and drift and are schematically shown in Fig. 1.1. Each of periodic
³⁷ these motions have a corresponding conserved quantity i.e. an adiabatic invariant.

The highest frequency periodic motion is gyration about a magnetic field of magnitude B . This motion is circular with a Larmor radius of

$$r = \frac{mv_{\perp}}{|q|B} \quad (1.2)$$

where m is the mass and v_{\perp} the particle's velocity perpendicular to \vec{B} . This motion

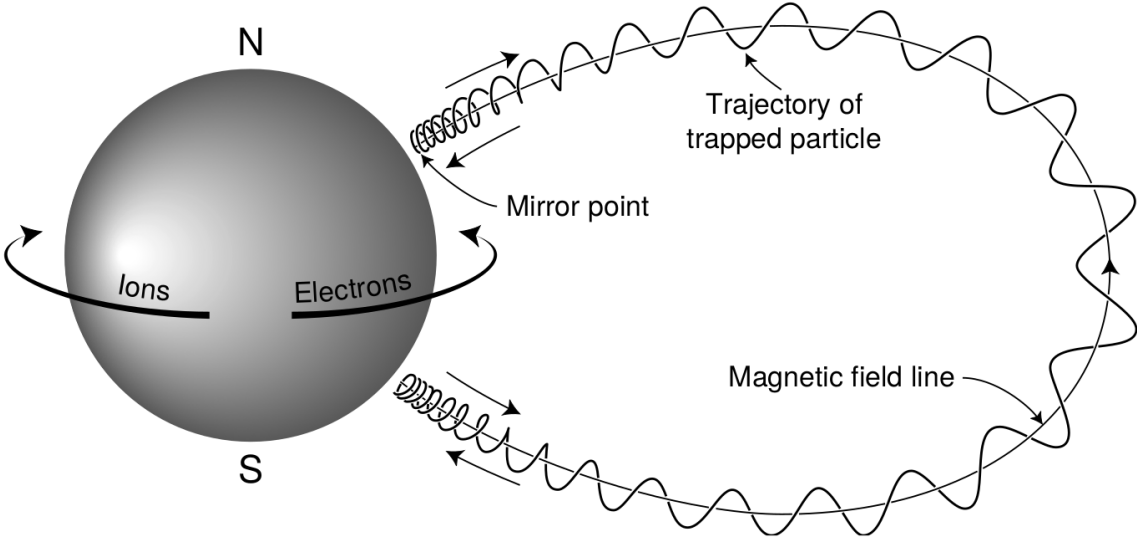


Figure 1.1: The three periodic motions of charged particles in Earth's dipole magnetic field. These motions are: gyration about the magnetic field line, bounce motion between the magnetic poles, and azimuthal drift around the Earth. Figure from (Baumjohann and Treumann, 1997).

has a corresponding gyrofrequency

$$\Omega = \frac{|q|B}{m} \quad (1.3)$$

in units of radians/second. Inside the radiation belts the electron gyrofrequency, Ω_e is on the order of a kHz. The corresponding adiabatic invariant is found by integrating the particle's canonical momentum around the particle's path of gyration

$$J_i = \oint (\vec{p} + q\vec{A}) \cdot d\vec{l} \quad (1.4)$$

³⁸ where J_i is the i^{th} adiabatic invariant and \vec{A} is the magnetic vector potential. This
³⁹ integral is carried out by integrating the first term over the circumference of the gyro
⁴⁰ orbit and integrating the second term using Stokes theorem to calculate the magnetic
⁴¹ flux enclosed by the gyro orbit. The gyration invariant is then $J_1 \sim v_{\perp}^2/B$, which is

⁴² conserved when the frequency, ω of a force acting on the gyrating electron satisfies
⁴³ $\omega \ll \Omega_e$.

⁴⁴ The second highest frequency periodic motion is bouncing due to a parallel
⁴⁵ gradient in \vec{B} . This periodic motion naturally arises in the magnetosphere because
⁴⁶ Earth's magnetic field is stronger near the poles, and artificially in the laboratory
⁴⁷ in magnetic bottle machines. To understand this motion we first we need to define
⁴⁸ the concept of pitch angle α as the angle between \vec{B} and \vec{v} which is schematically
⁴⁹ shown in Fig. 1.2a. The pitch angle relates v with v_{\perp} , and v_{\parallel} (the component of the
⁵⁰ particles velocity parallel to \vec{B}). As shown in 1.2b and c, a smaller (larger) α will
⁵¹ increase (decrease) the distance that the charged particle travels parallel to \vec{B} , during
⁵² one gyration.

Assuming the particle's kinetic energy is conserved, the conservation of J_1 implies that given a particle's $v_{\perp}(0)$ and $B(0)$ at the magnetic equator (where Earth's magnetic field is usually at a minimum), we can calculate its $v_{\perp}(s)$ along the particle's path s by calculating $B(s)$ from magnetic field models. The particle's perpendicular velocity is then related via

$$\frac{v_{\perp}^2(0)}{B(0)} = \frac{v_{\perp}^2(s)}{B(s)} \quad (1.5)$$

⁵³ which can be rewritten as

$$\frac{v^2 \sin^2 \alpha(0)}{B(0)} = \frac{v^2 - v_{\parallel}^2(s)}{B(s)} \quad (1.6)$$

⁵⁴ and re-arranged to solve for $v_{\parallel}(s)$

$$v_{\parallel}(s) = v \sqrt{1 - \frac{B(s)}{B(0)} \sin^2 \alpha(0)} \quad (1.7)$$

⁵⁵ which will tend towards 0 when the second term in the radical approaches 1.

56 The location where $v_{||}(s) = 0$ is called the mirror point and is where a particle
 57 reverses direction. Since Earth's magnetic field is stronger towards the poles, the
 58 mirroring particle will execute periodic bounce motion between its two mirror points
 59 in the northern and southern hemispheres. The corresponding adiabatic invariant, J_2
 60 is

$$J_2 = \oint p_{||} ds \quad (1.8)$$

where ds describes the particle path between the mirror points in the northern and southern hemispheres (see Fig. 1.1). J_2 is found by substituting Eq. 1.7 into Eq. 1.8 and defining the magnetic field strength at the mirror points as B_m where $\alpha(m) = 90^\circ$.

The J_2 integral can be written as

$$J_2 = 2p \int_{m_n}^{m_s} \sqrt{1 - \frac{B(s)}{B(m)}} ds \quad (1.9)$$

61 where m_n and m_s are the northern and southern mirror points, respectively. The
 62 bounce period can be estimated (e.g. Baumjohann and Treumann, 1997) to be

$$t_b \approx \frac{LR_e}{\sqrt{W/m}} (3.7 - 1.6 \sin \alpha(0)) \quad (1.10)$$

63 where L is the L -shell which describes the distance from the Earth's center to the
 64 location where a particular magnetic field line crosses the magnetic equator, in units
 65 of Earth radii, R_e . W is the particle's kinetic energy. As with gyration, the particle
 66 will bounce between the mirror points as long as $\omega \ll \Omega_b$, where Ω_b is the bounce
 67 frequency.

68 At this stage it is instructional to introduce the notion of the loss cone pitch
 69 angle, α_L . A particle with $\alpha \leq \alpha_L$ will mirror at or below ≈ 100 km altitude in the

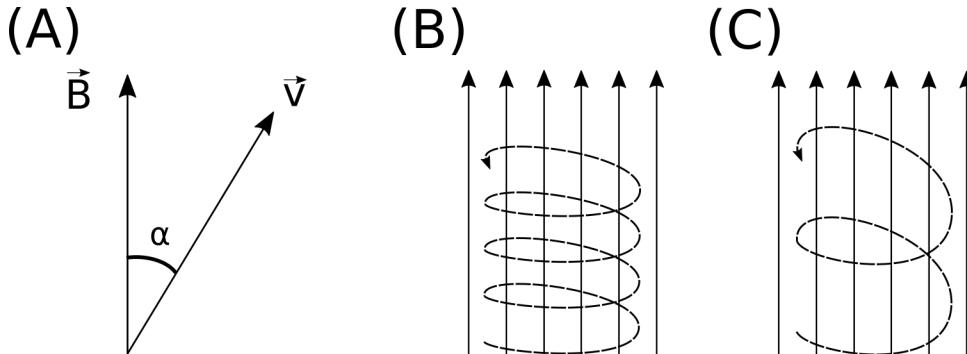


Figure 1.2: Charged particle motion in a uniform magnetic field \vec{B} . Panel (A) shows the geometry defining the pitch angle, α . Panel (B) and (C) show two helical electron trajectories with dashed lines assuming a large and small α (corresponding to a small and large parallel velocity $v_{||}$), respectively.

70 atmosphere. A particle at those altitudes will encounter Earth's atmosphere and has
 71 a significant probability of Coulomb scattering with atmospheric particles and be lost
 72 to the atmosphere.

73 The slowest periodic motion experienced by charged particles in Earth's mag-
 74 netic field is azimuthal drift around the Earth. This drift results from a combination of
 75 a radial gradient in \vec{B} and the curvature of the magnetic field. The radial gradient drift
 76 arises because Earth's magnetic field is stronger near the Earth where the particle's
 77 gyroradius radius of curvature is smaller as it gyrates towards stronger magnetic field,
 78 and larger when it gyrates outward. The overall effect is the particle gyro orbit does
 79 not close on itself and negatively charged particles drift East and positively charged
 80 particles drift West. The radial gradient drift is enhanced by the centrifugal force that
 81 a particle experiences as it bounces along the curved field lines. The drift adiabatic
 82 invariant, J_3 is found by integrating Eq. 1.4 over the complete particle orbit around
 83 the Earth. The shape of this drift orbit is otherwise known as a drift shell. For J_3 ,
 84 the first term is negligible and the second term is the magnetic flux enclosed by the
 85 drift shell, Φ_m i.e. $J_3 \sim \Phi_m$.

86 Figure 1.3 from Schulz and Lanzerotti (1974) shows contours of the gyration,
 87 bounce, and drift frequencies for electrons and protons in Earth's dipole magnetic
 88 field.

Up until now we have considered the three periodic motions due Earth's magnetic field and the absence of electric fields. If \vec{E} is present, a particle's center of gyration i.e., averaged position of the particle over a gyration, will drift with a velocity perpendicular to both \vec{E} and \vec{B} . The drift velocity can be solved directly from Eq. 1.1 and is

$$\vec{v}_E = \frac{\vec{E} \times \vec{B}}{B^2}. \quad (1.11)$$

89 Lastly, for more detailed derivations of these motions, see the following texts:
 90 Baumjohann and Treumann (1997); Schulz and Lanzerotti (1974); Tsurutani and
 91 Lakhina (1997).

92 Particle Populations and Their Interractions in the Magnetosphere

93 The single-particle motion in Earth's magnetic field described in the previous
 94 section is a prerequisite to understanding how magnetospheric particles organize into
 95 macroscopic populations. The structure of the outer magnetosphere is shown in Fig.
 96 1.4 and inner magnetosphere in Fig. 1.5. In this section we will introduce the various
 97 particle populations in the magnetosphere and how they couple.

98 The sun and its solar wind are ultimately the source of energy input into the
 99 magnetosphere. The solar wind at Earth's orbit is a plasma traveling at supersonic
 100 speeds with an embedded interplanetary magnetic field (IMF). When the solar wind
 101 encounters Earth's magnetic field the plasma can not easily penetrate into the
 102 magnetosphere, rather it drapes around the magnetosphere forming a cavity in the
 103 solar wind that is roughly shaped as shown in Fig. 1.4. Because the solar wind is

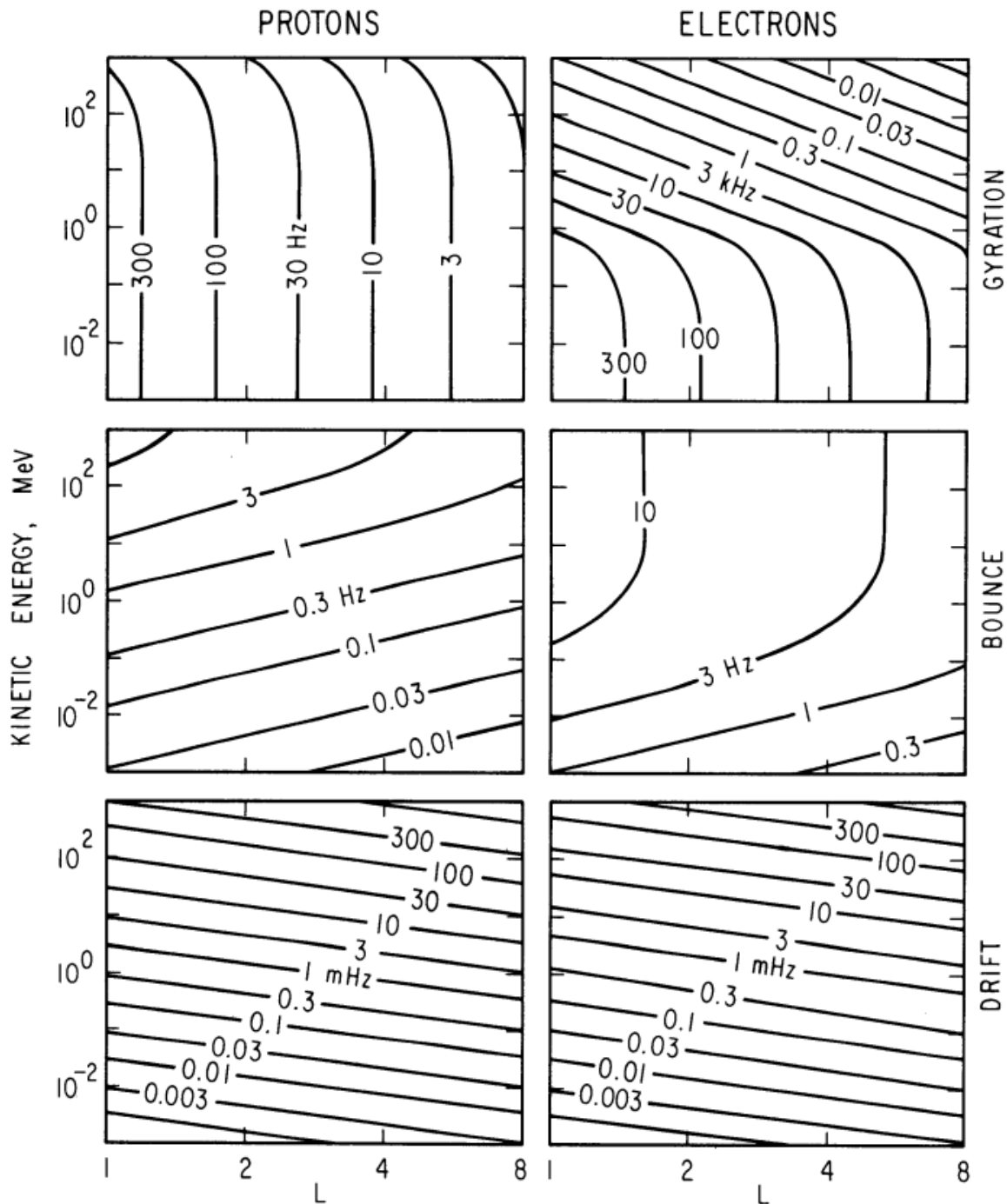


Figure 1.3: Contours of constant gyration, bounce, and drift frequencies for electrons and protons in a dipole field. Figure from Schulz and Lanzerotti (1974).

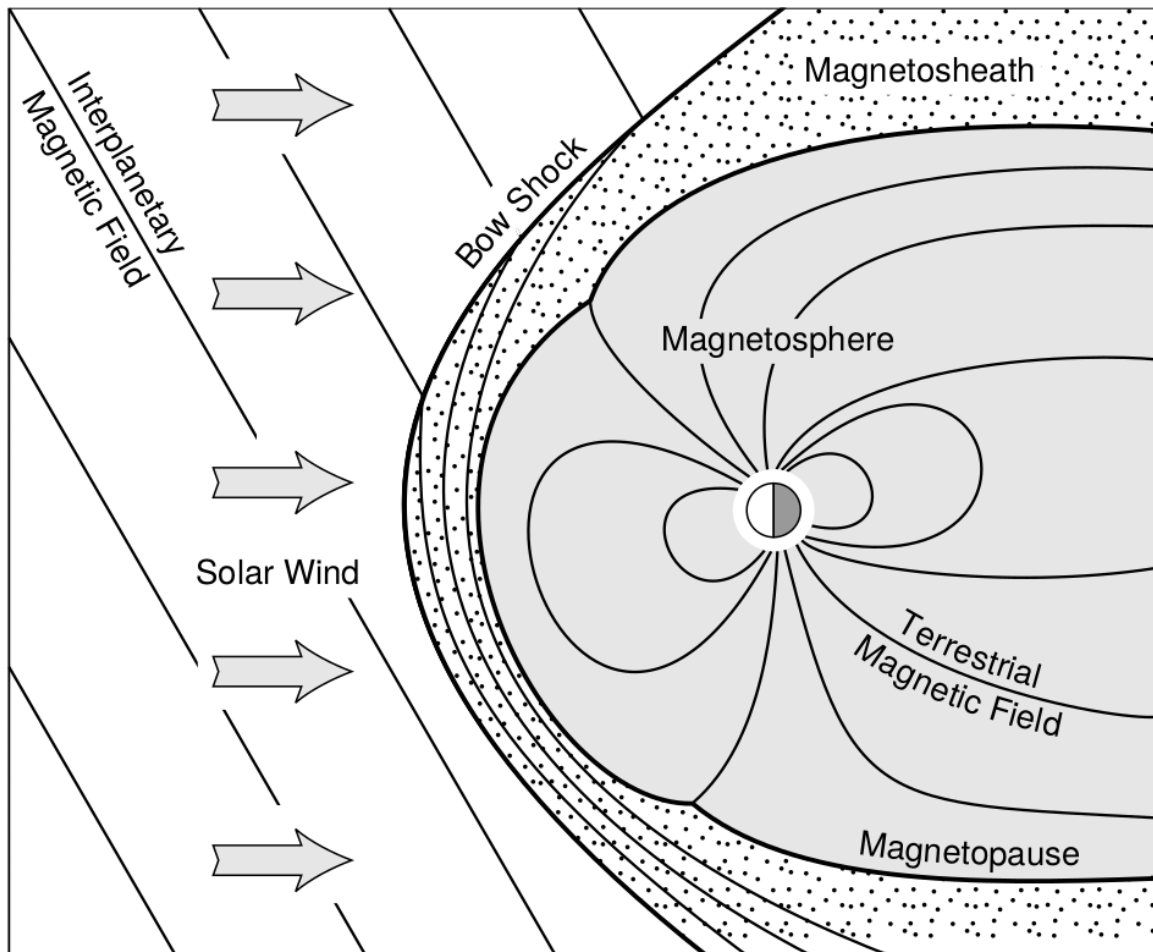


Figure 1.4: Macroscopic structures in the outer magnetosphere. The solar wind with its frozen-in interplanetary magnetic field is shown on the left and is traveling supersonically towards the right. The solar wind envelops Earth's magnetic field to create the magnetosphere cavity. Since the solar wind is traveling supersonically, it creates a bow shock up stream. Downstream of the bow shock the shocked solar wind plasma inside the magnetosheath flows around the magnetopause, a boundary between the solar wind and magnetosphere. Figure from Baumjohann and Treumann (1997).

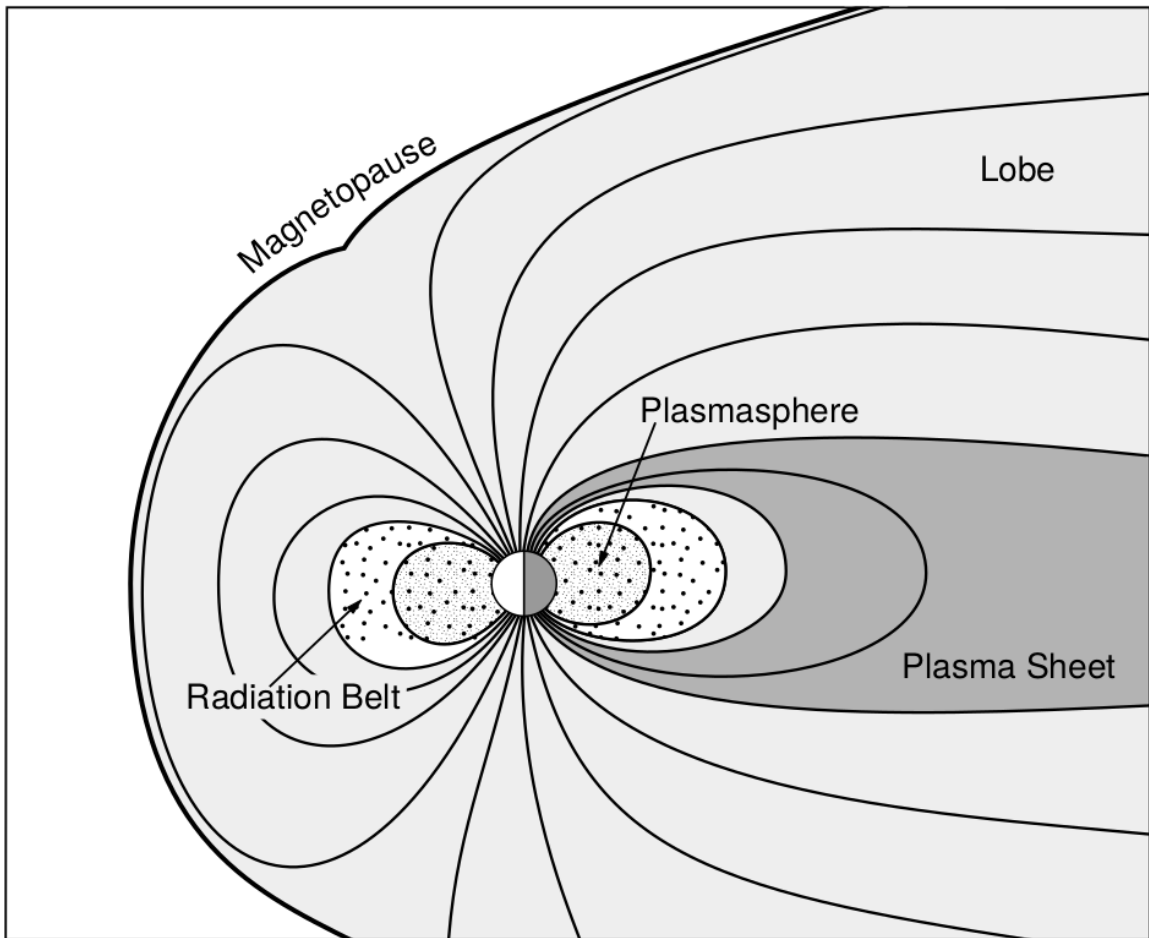


Figure 1.5: Macroscopic structures in the inner magnetosphere most relevant to this dissertation. The plasmasphere, and the radiation belts are shown and ring current is co-located there as well. Sun is to the left. Figure from Baumjohann and Treumann (1997).

104 supersonic at 1 AU, a bow shock exists upstream of the magnetosphere. The solar
 105 wind plasma, after it is shocked by the bow shock, flows around the magnetosphere
 106 inside the magnetosheath. The surface where the solar wind ram pressure and Earth's
 107 magnetic pressure balance is termed the magnetopause, which can be thought of as
 108 a boundary between the solar wind's and Earth's plasma environments. This is
 109 a slightly naive description of the magnetopause, but is nonetheless an instructive
 110 conceptual picture. The shocked plasma then flows past the Earth where it shapes
 111 the magnetotail. In the magnetotail the solar wind magnetic pressure balances Earth's
 112 magnetic field pressure in the lobes. The magnetotail extends on the order of 100
 113 R_E downstream of Earth [Add citation](#), and the tailward stretching of magnetic field
 114 lines creates the plasma sheet which exists in the region of low magnetic field strength
 115 near the magnetic equator [Add citation](#). The plasma sheet flows from dusk to dawn
 116 (out of the page in Figs. 1.4 and 1.5) and this current is connected to a zoo of other
 117 currents in the magnetosphere which is beyond the scope of this dissertation.

118 The idea of the magnetopause as a barrier between the solar wind and
 119 the magnetosphere is not entirely accurate due to the presence of reconnection.
 120 Reconnection was first conceived by Dungey (1961) who described the convection of
 121 Earth's magnetic field between the bow and tail regions of the magnetosphere. This
 122 process is known as the Dungey cycle and is most effective when the IMF is pointing
 123 southward as is shown in Fig. 1.6 part 1. As the IMF contacts Earth's magnetic
 124 field it reconnects with it so that Earth's magnetic field is directly connected to the
 125 IMF. Then as the solar wind flows tailward the IMF drags Earth's magnetic field
 126 towards the magnetotail as shown in Fig. 1.6 parts 2-6. As more and more magnetic
 127 field lines are draped in the magnetotail, magnetic pressure increases in the lobes
 128 which squeezes the plasma sheet until Earth's magnetic field reconnects as is shown
 129 in Fig. 1.6 part 7. Lastly, Fig. 1.6 part 8 shows the newly merged magnetic field

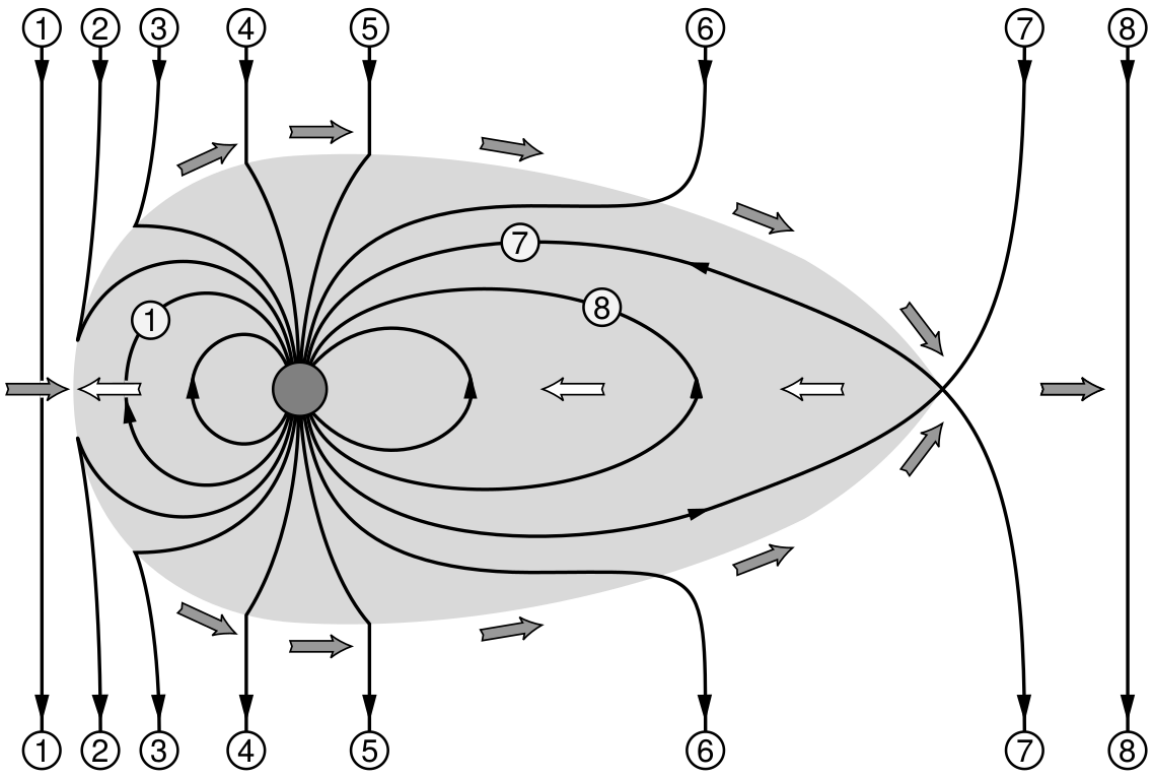


Figure 1.6: The series of steps involved in magnetic reconnection with a southward IMF. Figure from Baumjohann and Treumann (1997).

130 line and the plasma frozen on it moves Earthward under the magnetic tension force
 131 to become more dipolar. This is called a dipolarization of the magnetic field, and the
 132 plasma frozen on these field lines can be observed as injections (e.g. Turner et al.,
 133 2015). Injection of plasma into the inner magnetosphere is one of the drivers of inner
 134 magnetosphere dynamics. Should I talk about the K-H instability and how there
 135 could be micro reconnection? i.e. cite a paper or two that support or refute that
 136 idea.

137 Inner Magnetosphere Populations

138 Before we describe the inner magnetosphere particle populations, we first need to
 139 describe the coordinate system used to organize the inner magnetosphere populations.

140 The first coordinate was defined in section 1 and is the L shell. L shell can be thought
 141 of as an analogue to a radius but in a dipole geometry. The azimuthal coordinate
 142 is the magnetic local time (MLT). For an observer above Earth's north pole looking
 143 down, MLT is defined to be 0 (midnight) in the anti-sunward direction, and increases
 144 in the counter-clockwise direction with 6 at dawn, 12 at noon (sunward direction),
 145 and 18 in dusk. The last coordinate used in this dissertation is the magnetic latitude,
 146 λ which is analogous to the latitude coordinate and is defined to be 0 at the magnetic
 147 equator.

148 The low energy particle dynamics in the inner magnetosphere are organized by
 149 two electric fields: the co-rotation and the dawn-dusk electric fields. The co-rotation
 150 electric field arises from the rotation of Earth's magnetic field. Since particles are
 151 frozen on magnetic field lines and the plasma conductivity is effectively infinite, to
 152 a non-rotating observer, Earth's rotation appears as a radial electric field that drops
 153 off as $\sim L^2$. This electric field makes particles orbit around the Earth due to the
 154 $\vec{E} \times \vec{B}$ drift. The other electric field, pointing from dawn to dusk is called the
 155 convection electric field and is formed by the Earthward transport of particles from
 156 the magnetotail that appears as an electric field to a stationary observer (with respect
 157 to Earth). The superposition of the co-rotation and convection electric fields
 158 results in a potential field shown in Fig. 1.7. The shaded area in Fig. 1.7 shows
 159 the orbits on which low energy electrons are trapped, and outside are the untrapped
 160 particles. The dynamic topology of the shaded region in Fig. 1.7 is controlled by only
 161 the convection electric field which is dependent on the solar wind speed and the IMF.
 162 The lowest energy particles, that are most effected by these electric fields, make up
 163 the plasmasphere.

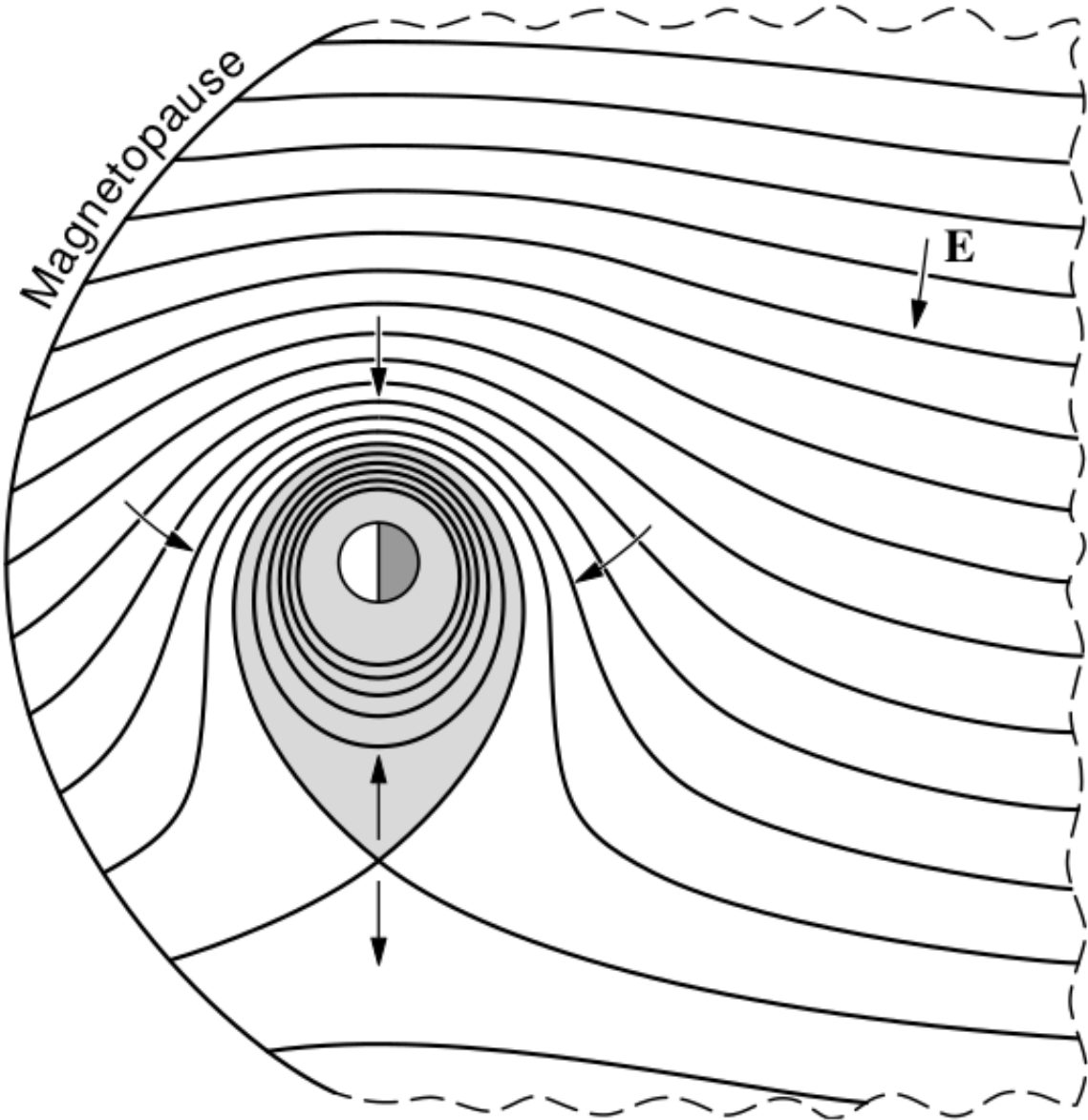


Figure 1.7: Equipotential lines and electric field arrows due to the superposition of the co-rotation and convection electric fields. Electrons in the shaded region execute closed orbits. Outside of the shaded regions the electrons are not trapped and will escape. The region separating the two regimes is called the Alfvén layer. Figure from Baumjohann and Treumann (1997).

¹⁶⁴ Plasmasphere The plasmasphere is a dense ($n_e \sim 10^3/\text{cm}^3$), cool plasma
¹⁶⁵ ($\sim \text{eV}$) that extends to $L \sim 4$ (extent is highly dependent on the solar wind and
¹⁶⁶ magnetospheric conditions) and is sourced from the ionosphere. The two main
¹⁶⁷ mechanisms that source the cold plasma from the ionosphere are ultraviolet ionization
¹⁶⁸ by sunlight and particle precipitation. The ultraviolet ionization by sunlight is
¹⁶⁹ strongly dependent on the time of day (day vs night), latitude (more ionization near
¹⁷⁰ the equator). The ionization due to particle precipitation, on the other hand, is highly
¹⁷¹ dependent on magnetospheric conditions, and mostly occurs at high latitudes.

¹⁷² The outer boundary of the plasmasphere is the plasmapause which is typically
¹⁷³ identified as a steep radial gradient in plasma density from $\sim 10^3/\text{cm}^3$ to $\sim 1/\text{cm}^3$. As
¹⁷⁴ we will see throughout this dissertation, the location of the plasmapause is important
¹⁷⁵ to model (e.g. O'Brien and Moldwin, 2003) and understand since the plasma density
¹⁷⁶ strongly controls the efficiency of particle scattering (Horne et al., 2005).

¹⁷⁷ Ring Current The next higher energy population is the ring current. This
¹⁷⁸ population consists of protons and electrons between tens and a few hundred keV
¹⁷⁹ that drift around the Earth. The orbits of higher energy particles are not as effected
¹⁸⁰ by the convection and co-rotation electric field, rather they drift around the Earth
¹⁸¹ due to gradient and curvature drifts. Since the direction of the drift is dependent on
¹⁸² charge, protons drift west around the Earth and electrons drift East. This has the
¹⁸³ effect of creating a current around the Earth.

¹⁸⁴ The ring current generates a magnetic field which decreases the magnetic field
¹⁸⁵ strength on Earth's surface and increases it outside of the ring current. The decrease
¹⁸⁶ of Earth's magnetic field strength is readily observed by a system of ground-based
¹⁸⁷ magnetometers and is merged into a Disturbance Storm Time (DST) index. An
¹⁸⁸ example of a DST index time series from a coronal mass ejection (CME) driven 2015

189 St. Patrick's Day storm is shown in Fig. 1.8. The ring current is sometimes first
 190 depleted and DST increases slightly (initial phase or sudden storm commencement).
 191 Then the ring current is rapidly built up during which DST rapidly decreases (main
 192 phase). Lastly the ring current gradually decays toward its equilibrium state over a
 193 period of a few days and DST increases towards 0 (recovery phase). The DST index
 194 along with other indices are readily used by the space physics community to quantify
 195 the global state of the magnetosphere.

196 Radiation Belts The highest energy particle populations are in the Van Allen
 197 radiation belts. These belts were discovered by Van Allen (1959) and Vernov and
 198 Chudakov (1960) during the Cold War and are a pair of toroidally shaped populations
 199 of trapped electrons and protons usually within to $L < 8$ and are shown in Fig. 1.9.
 200 Their quiescent toroidal shape is similar to the shape of the plasmasphere and ring
 201 current and is a result of Earth's dipole magnetic field and the conservation of the
 202 three adiabatic invariants discussed in section 1.

203 The inner radiation belt is extremely stable on time periods of years, extends
 204 to $L \approx 2$, and mainly consists of protons with energies between MeV and GeV and
 205 electrons with energies up to ≈ 1 MeV (Claudepierre et al., 2019). The source of
 206 inner radiation belt protons is believed to be due to cosmic-ray albedo neutron decay
 207 (e.g. Li et al., 2017) and inward radial diffusion for electrons (e.g. O'Brien et al.,
 208 2016). The gap between the inner and outer radiation belt is called the slot, which is
 209 believed to be due to hiss waves inside the plasmasphere (described below) scattering
 210 particles into the atmosphere (e.g. Breneman et al., 2015; Lyons and Thorne, 1973).

211 The outer radiation belt, on the other hand is much more dynamic and consists
 212 of mainly electrons of energies up to a few MeV. The outer belt's spatial extent is
 213 highly variable e.g. see Fig. 1.10, and is typically observed at $4 < L < 8$. Since

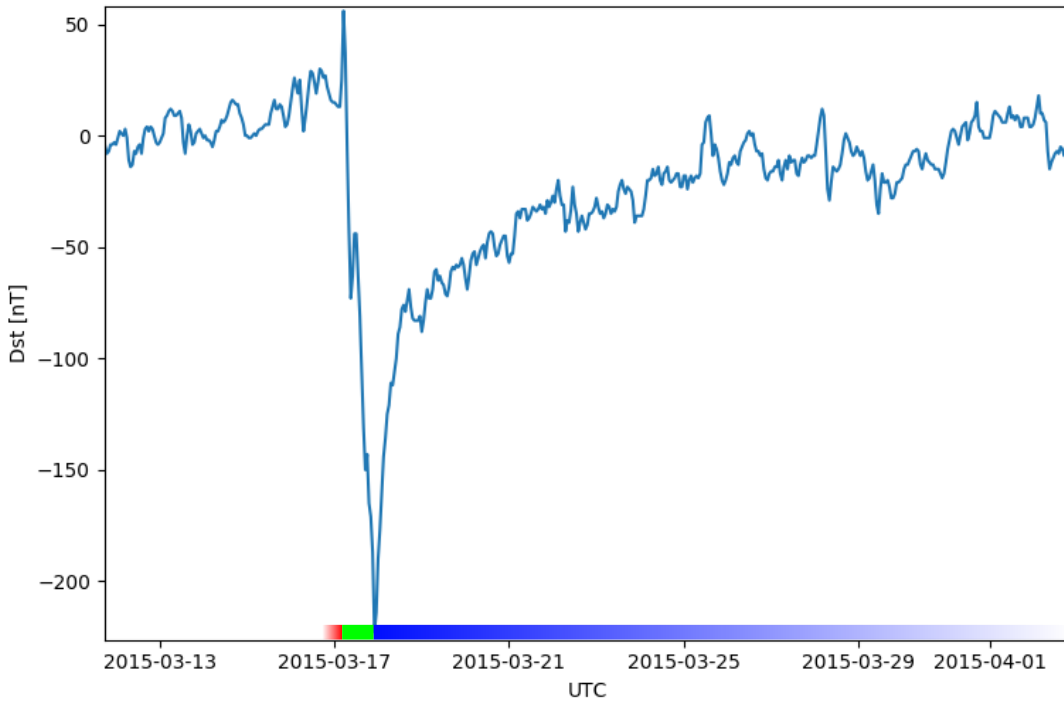


Figure 1.8: The DST index during the St. Patrick's Day 2015 storm. This storm was caused by a coronal mass ejection on March 15th, 2015. The storm phases are: initial phase, main phase, and recovery phase. The initial phase occurred when the Dst peaked at +50 nT on March 17th during which the ring current was eroded by the coronal mass ejection during the interval shown by the red bar. Then the rapid decrease to ≈ -200 nT was during the main phase where many injections from the magnetotail pumped up the ring current which reduced Earth's magnetic field strength at the ground and is shown with the green bar. Lastly, the recovery phase lasted from March 18th to approximately March 29th during which the ring current particles were lost and the ring current returned to its equilibrium state. The recovery phase is shown with the blue bar.

The Earth's Electron Radiation Belts

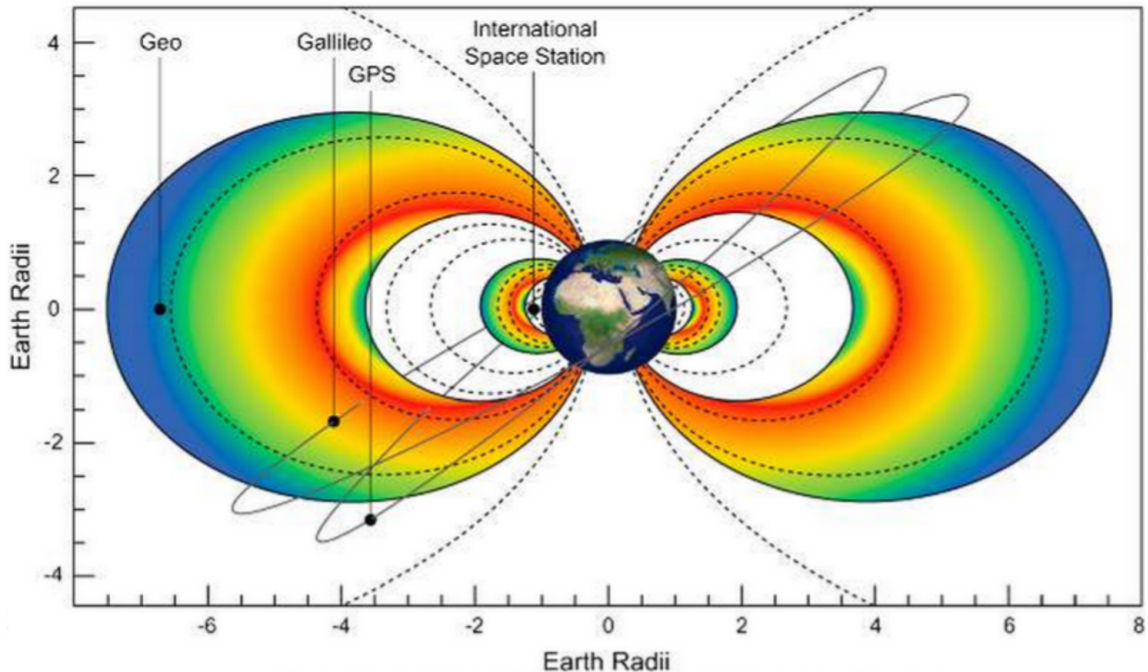


Figure 1.9: The two radiation belts with the locations of various satellites and orbits.
Figure from (Horne et al., 2013).

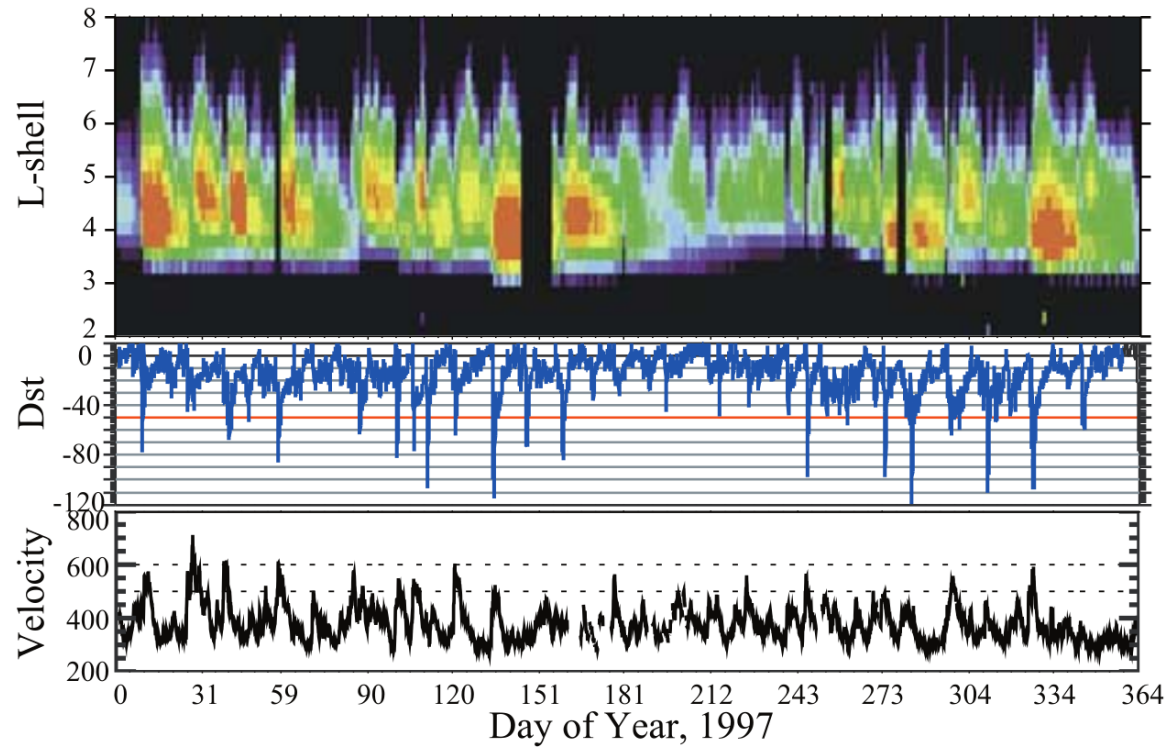


Figure 1.10: The dynamics of the outer radiation belt in 1997 from the POLAR satellite. Top panel shows the 1.2-2.4 MeV electron flux as a function of L and 1997 day of year. The middle panel shows the DST index, and bottom panel shows the solar wind velocity. Figure from (Reeves et al., 2003).

214 the outer radiation belt contains a dynamic population of energetic particles that
 215 pose a threat to human and technological presence in Earth's atmosphere and space,
 216 decades of research has been undertaken to understand and predict the outer radiation
 217 belt particles, waves, and wave-particle interactions. The dynamics of the outer
 218 radiation belt can be understood by considering various competing acceleration and
 219 loss mechanisms which will be described in the following sections.

220 Radiation Belt Particle Sources and Sinks

221 Adiabatic Heating

222 One of the particle heating and transport mechanisms arises from the Earthward
 223 convection of particles. The conservation of J_1 implies that the initial and final v_\perp
 224 depends on the change in the magnetic field amplitude

$$\frac{v_{\perp i}^2}{B_i} = \frac{v_{\perp f}^2}{B_f}. \quad (1.12)$$

225 As a particle convects Earthward, $B_f > B_i$ thus v_\perp must increase. The dipole
 226 magnetic field amplitude can be written as

$$B(L, \theta) = \frac{31.2 \mu\text{T}}{L^3} \sqrt{1 + 3 \cos^2 \theta} \quad (1.13)$$

227 which implies that

$$\frac{v_{\perp f}^2}{v_{\perp i}^2} = \left(\frac{L_i}{L_f} \right)^3. \quad (1.14)$$

228 .

229 In addition, as the particle convects Earthward the distance between the
 230 particle's mirror points decrease. If J_2 is conserved, the shrinking bounce path implies

²³¹ that v_{\parallel} must increase by

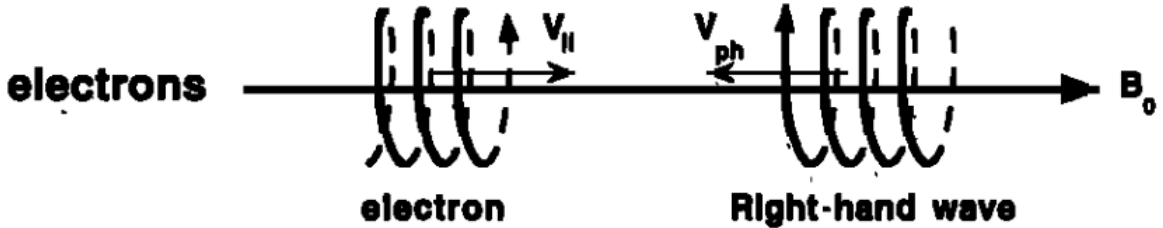
$$\frac{v_{\parallel f}^2}{v_{\parallel i}^2} = \left(\frac{L_i}{L_f} \right)^k \quad (1.15)$$

²³² where k ranges from 2 for equatorial pitch angles, $\alpha_{eq} = 0^\circ$, to 2.5 for $\alpha_{eq} = 90^\circ$
²³³ (Baumjohann and Treumann, 1997). Since the rate of adiabatic heating is greater in
²³⁴ the perpendicular direction than heating in the parallel direction, an initially isotropic
²³⁵ particle distribution will become anisotropic during its convection. These isotropic
²³⁶ particles can then become unstable to wave growth and generate waves in order to
²³⁷ reach equilibrium.

²³⁸ Wave Resonance Heating

²³⁹ Another mechanism that heats particles is due to particles resonating with
²⁴⁰ plasma waves. A few of the electromagnetic wave modes responsible for particle
²⁴¹ acceleration (and deceleration) relevant to radiation belt dynamics are hiss, whistler
²⁴² mode chorus (chorus), and electromagnetic ion cyclotron (EMIC) waves. These waves
²⁴³ are created by the loss cone instability that driven by an anisotropy of electrons
²⁴⁴ for chorus waves, and protons for EMIC waves. The level of anisotropy can be
²⁴⁵ quantified by the ratio of the perpendicular to parallel particle temperatures (T_{\perp}/T_{\parallel}).
²⁴⁶ A particle distribution is unstable when $T_{\perp}/T_{\parallel} > 1$ which facilitates wave growth.
²⁴⁷ Since electrons gyrate in a right-handed sense, the chorus waves also tend to be right
²⁴⁸ hand circularly polarized (Tsurutani and Lakhina, 1997). The same argument applies
²⁴⁹ to protons and left hand circularly polarized EMIC waves as well.

²⁵⁰ These circularly polarized waves can resonate with electrons and/or protons
²⁵¹ when their combined motion results in a static \vec{E} . One example of a resonance
²⁵² between a right hand circularly polarized wave and an electron is shown in Fig. 1.21
²⁵³ and is termed the cyclotron resonance. An electron's v_{\parallel} and the wave's parallel wave



$$\omega + \mathbf{k}_{\parallel} \mathbf{v}_{\parallel} = \Omega^-$$

Figure 1.11: The trajectories of an electron and a right-hand circularly polarized wave during a cyclotron resonance. The electron's v_{\parallel} and the wave's k_{\parallel} are in opposite directions such that the wave's frequency is Doppler shifted to an integer multiple of the electron cyclotron frequency. Figure from (Tsurutani and Lakhina, 1997).

vector, k_{\parallel} are in opposite directions such that the wave frequency ω is Doppler shifted to an integer multiple of the Ω_e at which point the electron feels a static electric field and is accelerated or decelerated. This acceleration happens when a resonance condition is satisfied between a wave and a particle for which we will now derive an illustrative toy model.

Assume a uniform magnetic field $\vec{B} = B_0 \hat{z}$ with a parallel propagating ($k = k \hat{z}$), right-hand circularly polarized wave. The wave's electric field as a function of position and time can be written as

$$\vec{E} = E_0 (\cos(\omega t - kz) \hat{x} + \sin(\omega t - kz) \hat{y}) \quad (1.16)$$

which is more clearly expressed by taking the dot product to find \vec{E} in the $\hat{\theta}$ direction

$$E_{\theta} = \vec{E} \times \hat{\theta} = E_0 \cos(\omega t - kz + \theta). \quad (1.17)$$

Now assume that the electron is traveling in the $-\hat{z}$ direction with a velocity $\vec{v} = -v_0 \hat{z}$

²⁶³ so its time dependent position along \hat{z} is

$$z(t) = -v_0 t \quad (1.18)$$

²⁶⁴ and gyrophase is

$$\theta(t) = -\Omega t + \theta(0) \quad (1.19)$$

²⁶⁵ where the first negative sign comes from the electron's negative charge. Now we put
²⁶⁶ this all together and express the electric field and the force that the electron will
²⁶⁷ experience

$$m \frac{dv_\theta}{dt} = qE_\theta = qE_0 \sin((\omega + kv_0 - \Omega)t + \theta(0)). \quad (1.20)$$

²⁶⁸ This is a relatively complex expression, but when the time dependent component,

$$\omega + kv_0 - \Omega = 0, \quad (1.21)$$

²⁶⁹ the electron will be in a static electric field which will accelerate or decelerate the
²⁷⁰ electron depending on θ_0 , the phase between the wave and the electron. **Show Bortnik
²⁷¹ 2008 plot?** The expression in Eq. 1.21 is commonly referred to as the resonance
²⁷² condition and is more generally written as

$$\omega - k_{||}v_{||} = \frac{n\Omega_e}{\gamma} \quad (1.22)$$

²⁷³ where n is the resonance order, and γ is the relativistic correction (e.g. Millan and
²⁷⁴ Thorne, 2007). In the case of the cyclotron resonance, $\omega \approx \Omega_e$ thus J_1 is violated.
²⁷⁵ Since J_1 is violated, J_2 and J_3 are also violated since the conditions required to
²⁷⁶ violate J_2 and J_3 are less stringent than J_1 . It is important to remember that along

277 the particle's orbit it will encounter and experience the effects of many waves along
 278 its orbit. The typical MLT extent of a handful of waves that are capable of resonating
 279 with radiation belt electrons are shown in Fig. 1.12.

280 Particle Losses

281 Now that we have seen two general mechanisms with which particles are
 282 accelerated and transported in the magnetosphere, we will now consider a few
 283 specific mechanisms with which particles are lost to the atmosphere or the solar
 284 wind. One particle loss mechanism into the solar wind is magnetopause shadowing
 285 (e.g. Ukhorskiy et al., 2006). Particles are sometimes lost when the ring current is
 286 strengthened and Earth's magnetic field strength is increased outside of the ring
 287 current (and reduced on Earth's surface). If the time scale of the ring current
 288 strengthening is slower than a particle drift, J_3 is conserved. Then in order to
 289 conserve J_3 while the magnetic field strength is increased, the particle's drift shell
 290 must move outward to conserve the magnetic flux contained by the drift shell. Then
 291 if the particle's drift shell expands to the point that it crosses the magnetopause, the
 292 particle will be lost to the solar wind.

293 **Move to acceleration?** Another particle loss and acceleration mechanism is driven
 294 by ultra low frequency (ULF) waves and is called radial diffusion. Radial diffusion is
 295 the transport of particles from high to low phase space density, f . If the transport is
 296 radially inward, particles will appear to be accelerated. On the other hand, radially
 297 outward radial diffusion can transport particles through the magnetopause where
 298 they will be lost to the solar wind. Reeves et al. (2013) investigated the driver of
 299 particle acceleration during the October 2012 storm and observationally found that
 300 inward radial diffusion was not dominant, rather local acceleration via wave-resonance
 301 heating (i.e. particle diffusion in pitch angle and energy which will be described below)

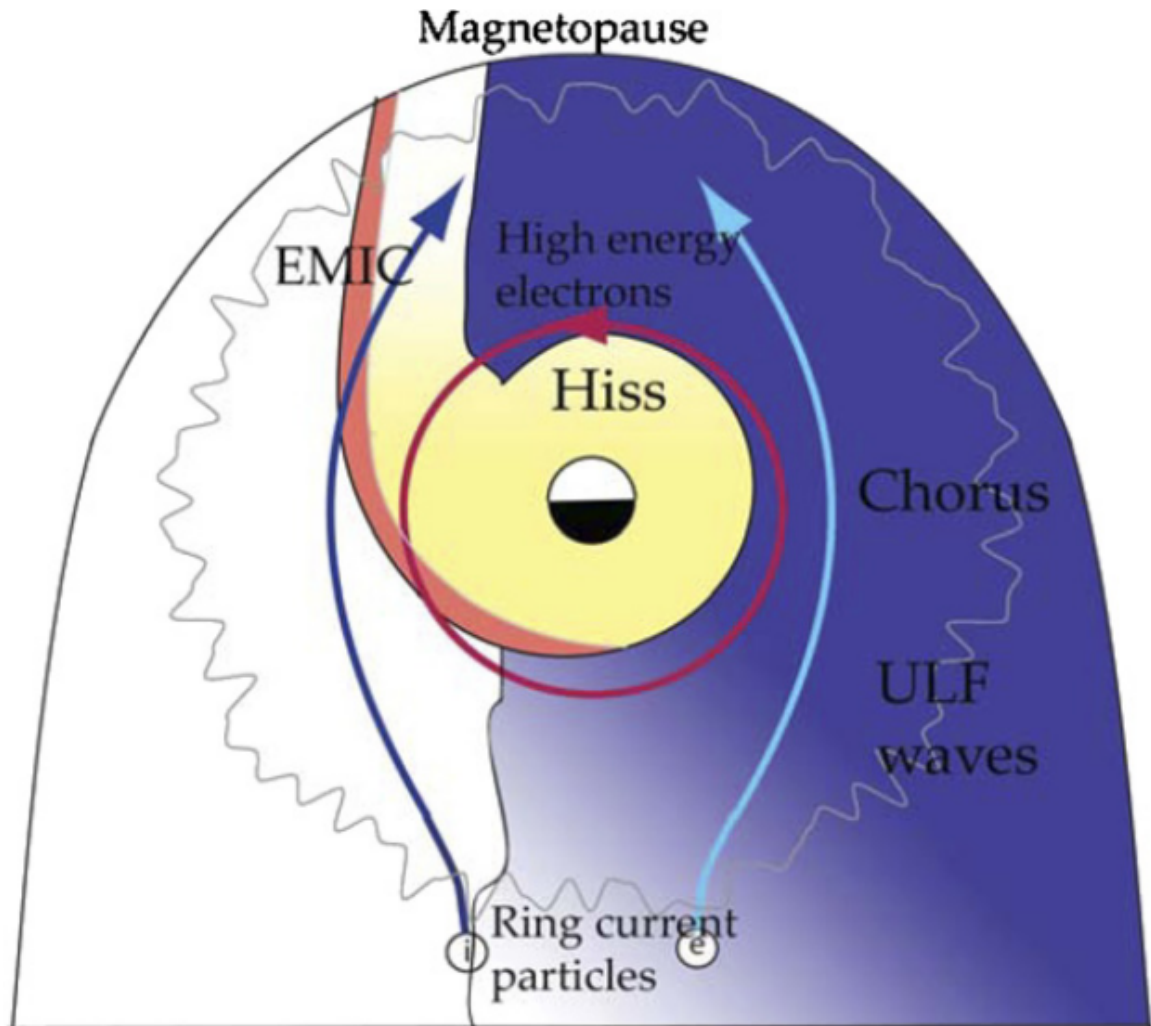


Figure 1.12: Various wave modes in the magnetosphere. Ultra low frequency waves occur through the magnetosphere. Chorus waves are typically observed in the 0-12 midnight-dawn region. EMIC waves are typically observed in the dusk MLT sector. Hiss waves are observed inside the plasmasphere. Figure from Millan and Thorne (2007).

302 appeared to be the dominant acceleration mechanism.

303 The loss mechanism central to this dissertation is pitch angle and energy
 304 scattering of electrons by waves. Some of the waves that scatter electrons in energy
 305 and pitch angle in the inner magnetosphere are: plasmaspheric hiss (e.g. Breneman
 306 et al., 2015; O'Brien et al., 2014), EMIC waves (e.g. Capannolo et al., 2019; Hendry
 307 et al., 2017), and chorus waves (e.g. Breneman et al., 2017; Kasahara et al., 2018;
 308 Ozaki et al., 2019). These wave-particle interactions occur when the resonance
 309 condition in Eq. 1.22 is satisfied at which point the particle's energy and α is modified
 310 by the wave. More details regarding the theory of pitch angle and energy diffusion is
 311 given in Chapter X. If the wave changes α towards 0 such that $\alpha < \alpha_{LC}$, the particle's
 312 mirror point lowers to less than 100 km altitude where the particle can be lost due
 313 collisions with air. One manifestation of pitch angle scattering of particles into the
 314 loss cone are microbursts: a sub-second durtaison impulse of electrons.

315

Microbursts

316 Microbursts were first identified in high altitude balloon observations of bremsstrahlung
 317 X-rays emitted by microburst electrons impacting the atmosphere by Anderson and
 318 Milton (1964). Since then, other balloons have observed microburst X-ray signatures
 319 in the upper atmosphere (e.g. Anderson et al., 2017; Barcus et al., 1966; Parks, 1967;
 320 Trefall et al., 1966; Woodger et al., 2015; ?). In addition to their X-ray signature,
 321 microbursts electrons have been directly observed in LEO with spacecraft including
 322 the Solar Anomalous and Magnetospheric Particle Explorer (SAMPEX), Focused
 323 Investigation of Relativistic Electron Bursts: Intensity, Range, and Dynamics II
 324 (FIREBIRD-II), Science Technologies Satellite (STSAT-I) (e.g. Blake et al., 1996;
 325 Blum et al., 2015; Breneman et al., 2017; Crew et al., 2016; Lee et al., 2012, 2005;
 326 Lorentzen et al., 2001a,b; Nakamura et al., 1995, 2000; O'Brien et al., 2004, 2003).

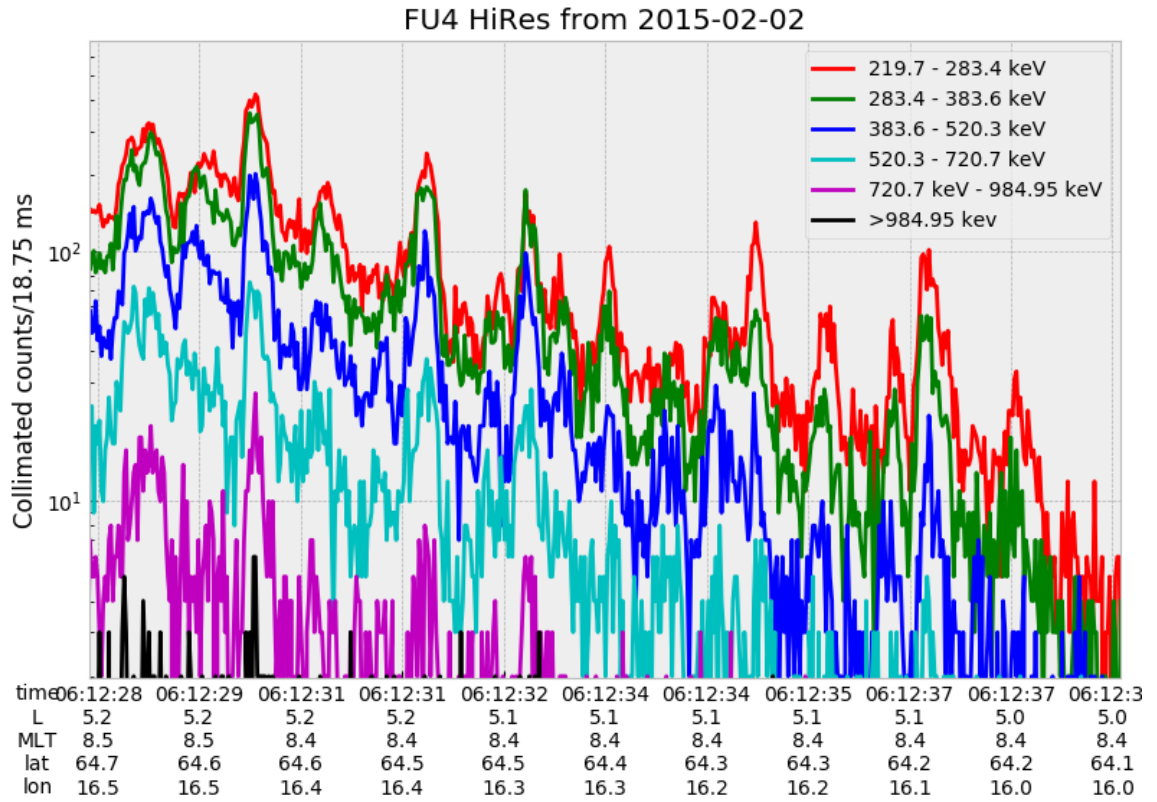


Figure 1.13: An example train of microbursts observed by FIREBIRD-II unit 4 on February 2nd, 2015. The colored curves show the differential energy channel count rates in six channels from ≈ 200 keV to greater than 1 MeV. The x-axis labels show auxiliary information such as time of observation and the spacecraft position in L, MLT, latitude and longitude coordinates.

327 An example microburst time series is shown in Fig. 1.13 and was observed by
 328 Montana State University's (MSU) FIREBIRD-II CubeSats. The prominent features
 329 of microbursts in Fig. 1.13 are their ≈ 1 second duration, half order of magnitude
 330 increase in count rate above the falling background, and their approximately 200-800
 331 keV energy extent.

332 Microbursts are observed on magnetic field footprints that are connected to the
 333 outer radiation belt (approximately $4 < L < 8$), and are predominately observed in

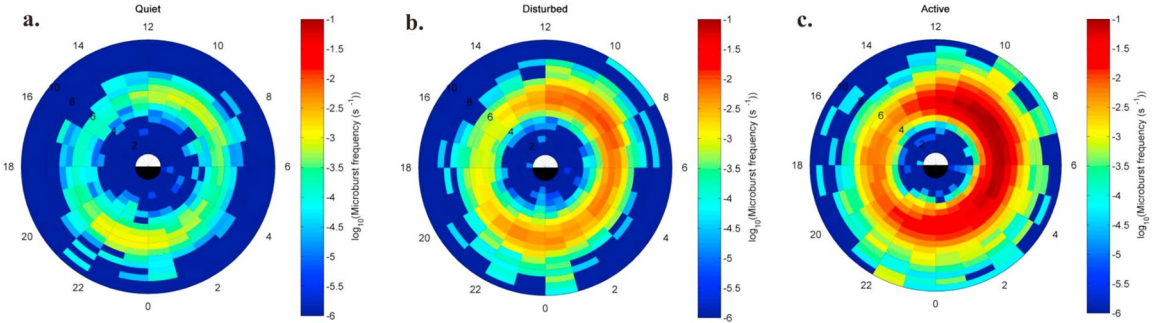


Figure 1.14: Relativistic ($> 1\text{MeV}$) distribution of microburst occurrence rates as a function of L and MLT. The three panels show the microburst occurrence rate dependence on geomagnetic activity, parameterized by the auroral electrojet (AE) index for (a) $\text{AE} < 100 \text{nT}$, (b) $100 < \text{AE} < 300 \text{nT}$ and (c) $\text{AE} > 300 \text{nT}$. Figure from Douma et al. (2017).

the 0-12 MLT sector with an elevated occurrence frequency during magnetospherically disturbed times as shown in Fig. 1.14. Microbursts have been previously observed over a wide energy range from a few tens of keV (Datta et al., 1997; Parks, 1967) to greater than 1 MeV (e.g. Blake et al., 1996; Greeley et al., 2019). The microburst electron flux (J) falls off in energy, and the microburst energy spectra is typically well fit to a decaying exponential

$$J(E) = J_0 e^{-E/E_0} \quad (1.23)$$

where J_0 is the flux at 0 keV (unphysical free parameter) and E_0 quantifies the efficiency of the scattering mechanism in energy (.e.g Datta et al., 1997; Lee et al., 2005; Parks, 1967). A small E_0 suggests that mostly low energy particles are scattered and a high E_0 suggests that the scattering mechanism scatters low and high energy electrons. Reality is a bit more messy and a high E_0 may be a signature of a scattering mechanism preferential to high energy electrons, but is hidden by the convolution of the source particles available to be scattered (typically with a falling energy spectrum)

347 and the energy-dependent scattering efficiency.

348 The short duration of microbursts observed by a single LEO satellite has an
349 ambiguity when interpreting what is exactly a microburst. The two possible realities
350 are: a microburst is very small and spatially stationary so that the LEO spacecraft
351 passes through it in less than a second. Alternatively, microbursts are spatially large
352 with a short duration such that the microburst passes by the spacecraft in a fraction
353 of a second. There are a few ways to distinguish between the two possible realities,
354 and each one has a unique set of advantages.

355 A high altitude balloon provides essentially a stationary view of the precipitating
356 particles under the radiation belt footprints so a short-lived, temporal microburst
357 can be unambiguously identified. Spatial structures on the other hand are difficult
358 to identify because a balloon is essentially still on drift timescales thus a variation in
359 the X-rays can be due to the spatial structure or an increase of precipitating particles
360 over the whole area. Furthermore, if the stationary structure is drifting its particles
361 are not precipitating into the atmosphere so there is no X-ray signature.

362 Another solution is multi-spacecraft missions that can determine if a microburst
363 is spatial or temporal. As will be shown in this dissertation, if a microburst is
364 observed simultaneously by two spacecraft then it is temporally transient and has
365 a size greater than the spacecraft separation. On the other hand, if two spacecraft
366 observe a microburst-like feature in the same location and at different times, then it is
367 spatial may be a curtain (Blake and O'Brien, 2016). Both observational methods have
368 a unique set of strengths, and this dissertation takes the multi-spacecraft approach
369 to identify and study microbursts.

370

Scope of Reserach

371 This dissertation furthers our understanding of the microburst scattering
372 mechanism by observing the scattering directly, and measuring the microburst sizes
373 and comparing them to the size of waves near the magnetic equator where those
374 electrons could have been scattered. Chapter **X** describes a microburst scattering
375 event observed by NASA's Van Allen Probes which was studied in the theoretic
376 framework of pitch angle and energy diffusion. The following two chapters will then
377 study the size of microbursts. Chapter **Y** describes a bouncing packet microburst
378 observation made by MSU's FIREBIRD-II mission where the microburst's lower
379 bound longitudinal and latitudinal sizes were estimated. Then Chapter **Z** expands
380 the case study from Ch. **Y** to a statistical study of microburst sizes using The
381 Aerospace Corporation's AeroCube-6 (AC6) CubeSats. In this study, a Monte Carlo
382 and analytic microburst size models were developed to account for the compounding
383 effects of random microburst sizes and locations. Lastly, Ch. **A** will summarize the
384 dissertation work and make concluding remarks regarding outstanding questions in
385 microburst physics.

- 387 Anderson, B., Shekhar, S., Millan, R., Crew, A., Spence, H., Klumpar, D., Blake, J.,
 388 O'Brien, T., and Turner, D. (2017). Spatial scale and duration of one microburst
 389 region on 13 August 2015. *Journal of Geophysical Research: Space Physics*.
- 390 Anderson, K. A. and Milton, D. W. (1964). Balloon observations of X rays in the
 391 auroral zone: 3. High time resolution studies. *Journal of Geophysical Research*,
 392 69(21):4457–4479.
- 393 Barcus, J., Brown, R., and Rosenberg, T. (1966). Spatial and temporal character of
 394 fast variations in auroral-zone x rays. *Journal of Geophysical Research*, 71(1):125–
 395 141.
- 396 Baumjohann, W. and Treumann, R. A. (1997). *Basic space plasma physics*. World
 397 Scientific.
- 398 Blake, J.,Looper, M., Baker, D., Nakamura, R., Klecker, B., and Hovestadt, D.
 399 (1996). New high temporal and spatial resolution measurements by sampex of the
 400 precipitation of relativistic electrons. *Advances in Space Research*, 18(8):171 – 186.
- 401 Blake, J. B. and O'Brien, T. P. (2016). Observations of small-scale latitudinal
 402 structure in energetic electron precipitation. *Journal of Geophysical Research: Space
 403 Physics*, 121(4):3031–3035. 2015JA021815.
- 404 Blum, L., Li, X., and Denton, M. (2015). Rapid MeV electron precipitation as
 405 observed by SAMPEX/HILT during high-speed stream-driven storms. *Journal of
 406 Geophysical Research: Space Physics*, 120(5):3783–3794. 2014JA020633.
- 407 Breneman, A., Crew, A., Sample, J., Klumpar, D., Johnson, A., Agapitov, O.,
 408 Shumko, M., Turner, D., Santolik, O., Wygant, J., et al. (2017). Observations
 409 directly linking relativistic electron microbursts to whistler mode chorus: Van allen
 410 probes and FIREBIRD II. *Geophysical Research Letters*.
- 411 Breneman, A. W., Halford, A., Millan, R., McCarthy, M., Fennell, J., Sample, J.,
 412 Woodger, L., Hospodarsky, G., Wygant, J. R., Cattell, C. A., et al. (2015). Global-
 413 scale coherence modulation of radiation-belt electron loss from plasmaspheric hiss.
 414 *Nature*, 523(7559):193.
- 415 Capannolo, L., Li, W., Ma, Q., Shen, X.-C., Zhang, X.-J., Redmon, R., Rodriguez,
 416 J., Engebretson, M., Kletzing, C., Kurth, W., et al. (2019). Energetic electron
 417 precipitation: multi-event analysis of its spatial extent during emic wave activity.
 418 *Journal of Geophysical Research: Space Physics*.
- 419 Claudepierre, S., O'Brien, T., Looper, M., Blake, J., Fennell, J., Roeder, J.,
 420 Clemmons, J., Mazur, J., Turner, D., Reeves, G., et al. (2019). A revised look

- 421 at relativistic electrons in the earth's inner radiation zone and slot region. *Journal
422 of Geophysical Research: Space Physics*, 124(2):934–951.
- 423 Crew, A. B., Spence, H. E., Blake, J. B., Klumpar, D. M., Larsen, B. A., O'Brien,
424 T. P., Driscoll, S., Handley, M., Legere, J., Longworth, S., Mashburn, K.,
425 Mosleh, E., Ryhajlo, N., Smith, S., Springer, L., and Widholm, M. (2016). First
426 multipoint in situ observations of electron microbursts: Initial results from the
427 NSF FIREBIRD II mission. *Journal of Geophysical Research: Space Physics*,
428 121(6):5272–5283. 2016JA022485.
- 429 Datta, S., Skoug, R., McCarthy, M., and Parks, G. (1997). Modeling of microburst
430 electron precipitation using pitch angle diffusion theory. *Journal of Geophysical
431 Research: Space Physics*, 102(A8):17325–17333.
- 432 Douma, E., Rodger, C. J., Blum, L. W., and Clilverd, M. A. (2017). Occurrence
433 characteristics of relativistic electron microbursts from SAMPEX observations.
434 *Journal of Geophysical Research: Space Physics*, 122(8):8096–8107. 2017JA024067.
- 435 Dungey, J. W. (1961). Interplanetary magnetic field and the auroral zones. *Phys.
436 Rev. Lett.*, 6:47–48.
- 437 Greeley, A., Kanekal, S., Baker, D., Klecker, B., and Schiller, Q. (2019). Quantifying
438 the contribution of microbursts to global electron loss in the radiation belts. *Journal
439 of Geophysical Research: Space Physics*.
- 440 Hendry, A. T., Rodger, C. J., and Clilverd, M. A. (2017). Evidence of sub-mev
441 emic-driven electron precipitation. *Geophysical Research Letters*, 44(3):1210–1218.
- 442 Horne, R., Glauert, S., Meredith, N., Boscher, D., Maget, V., Heynderickx, D., and
443 Pitchford, D. (2013). Space weather impacts on satellites and forecasting the earth's
444 electron radiation belts with spacecast. *Space Weather*, 11(4):169–186.
- 445 Horne, R. B., Thorne, R. M., Shprits, Y. Y., Meredith, N. P., Glauert, S. A., Smith,
446 A. J., Kanekal, S. G., Baker, D. N., Engebretson, M. J., Posch, J. L., et al.
447 (2005). Wave acceleration of electrons in the van allen radiation belts. *Nature*,
448 437(7056):227.
- 449 Kasahara, S., Miyoshi, Y., Yokota, S., Mitani, T., Kasahara, Y., Matsuda, S.,
450 Kumamoto, A., Matsuoka, A., Kazama, Y., Frey, H., et al. (2018). Pulsating
451 aurora from electron scattering by chorus waves. *Nature*, 554(7692):337.
- 452 Lee, J. J., Parks, G. K., Lee, E., Tsurutani, B. T., Hwang, J., Cho, K. S., Kim, K.-H.,
453 Park, Y. D., Min, K. W., and McCarthy, M. P. (2012). Anisotropic pitch angle
454 distribution of 100 keV microburst electrons in the loss cone: measurements from
455 STSAT-1. *Annales Geophysicae*, 30(11):1567–1573.

- 456 Lee, J.-J., Parks, G. K., Min, K. W., Kim, H. J., Park, J., Hwang, J., McCarthy,
 457 M. P., Lee, E., Ryu, K. S., Lim, J. T., Sim, E. S., Lee, H. W., Kang, K. I., and
 458 Park, H. Y. (2005). Energy spectra of 170–360 keV electron microbursts measured
 459 by the korean STSAT-1. *Geophysical Research Letters*, 32(13). L13106.
- 460 Li, X., Selesnick, R., Schiller, Q., Zhang, K., Zhao, H., Baker, D. N., and Temerin,
 461 M. A. (2017). Measurement of electrons from albedo neutron decay and neutron
 462 density in near-earth space. *Nature*, 552(7685):382.
- 463 Lorentzen, K. R., Blake, J. B., Inan, U. S., and Bortnik, J. (2001a). Observations
 464 of relativistic electron microbursts in association with VLF chorus. *Journal of
 465 Geophysical Research: Space Physics*, 106(A4):6017–6027.
- 466 Lorentzen, K. R.,Looper, M. D., and Blake, J. B. (2001b). Relativistic electron
 467 microbursts during the GEM storms. *Geophysical Research Letters*, 28(13):2573–
 468 2576.
- 469 Lyons, L. R. and Thorne, R. M. (1973). Equilibrium structure of radiation belt
 470 electrons. *Journal of Geophysical Research*, 78(13):2142–2149.
- 471 Millan, R. and Thorne, R. (2007). Review of radiation belt relativistic electron losses.
 472 *Journal of Atmospheric and Solar-Terrestrial Physics*, 69(3):362 – 377.
- 473 Nakamura, R., Baker, D. N., Blake, J. B., Kanekal, S., Klecker, B., and Hovestadt,
 474 D. (1995). Relativistic electron precipitation enhancements near the outer edge of
 475 the radiation belt. *Geophysical Research Letters*, 22(9):1129–1132.
- 476 Nakamura, R., Isowa, M., Kamide, Y., Baker, D., Blake, J., and Looper, M. (2000).
 477 Observations of relativistic electron microbursts in association with VLF chorus.
 478 *J. Geophys. Res*, 105:15875–15885.
- 479 O'Brien, T., Claudepierre, S., Blake, J., Fennell, J. F., Clemons, J., Roeder, J.,
 480 Spence, H. E., Reeves, G., and Baker, D. (2014). An empirically observed pitch-
 481 angle diffusion eigenmode in the earth's electron belt near $l^* = 5.0$. *Geophysical
 482 Research Letters*, 41(2):251–258.
- 483 O'Brien, T., Claudepierre, S., Guild, T., Fennell, J., Turner, D., Blake, J., Clemons,
 484 J., and Roeder, J. (2016). Inner zone and slot electron radial diffusion revisited.
 485 *Geophysical Research Letters*, 43(14):7301–7310.
- 486 O'Brien, T. and Moldwin, M. (2003). Empirical plasmapause models from magnetic
 487 indices. *Geophysical Research Letters*, 30(4).
- 488 O'Brien, T. P., Looper, M. D., and Blake, J. B. (2004). Quantification of relativistic
 489 electron microburst losses during the GEM storms. *Geophysical Research Letters*,
 490 31(4). L04802.

- 491 O'Brien, T. P., Lorentzen, K. R., Mann, I. R., Meredith, N. P., Blake, J. B., Fennell,
 492 J. F., Looper, M. D., Milling, D. K., and Anderson, R. R. (2003). Energization of
 493 relativistic electrons in the presence of ULF power and MeV microbursts: Evidence
 494 for dual ULF and VLF acceleration. *Journal of Geophysical Research: Space
 495 Physics*, 108(A8).
- 496 Ozaki, M., Miyoshi, Y., Shiokawa, K., Hosokawa, K., Oyama, S.-i., Kataoka, R.,
 497 Ebihara, Y., Ogawa, Y., Kasahara, Y., Yagitani, S., et al. (2019). Visualization of
 498 rapid electron precipitation via chorus element wave-particle interactions. *Nature
 499 communications*, 10(1):257.
- 500 Parks, G. K. (1967). Spatial characteristics of auroral-zone X-ray microbursts. *Journal
 501 of Geophysical Research*, 72(1):215–226.
- 502 Reeves, G., Spence, H. E., Henderson, M., Morley, S., Friedel, R., Funsten, H., Baker,
 503 D., Kanekal, S., Blake, J., Fennell, J., et al. (2013). Electron acceleration in the
 504 heart of the van allen radiation belts. *Science*, 341(6149):991–994.
- 505 Reeves, G. D., McAdams, K. L., Friedel, R. H. W., and O'Brien, T. P. (2003). Ac-
 506 celeration and loss of relativistic electrons during geomagnetic storms. *Geophysical
 507 Research Letters*, 30(10):n/a–n/a. 1529.
- 508 Schulz, M. and Lanzerotti, L. J. (1974). *Particle Diffusion in the Radiation Belts*.
 509 Springer.
- 510 Trefall, H., Bjordal, J., Ullaland, S., and Stadsnes, J. (1966). On the extension of
 511 auroral-zone x-ray microbursts. *Journal of Atmospheric and Terrestrial Physics*,
 512 28(2):225–233.
- 513 Tsurutani, B. T. and Lakhina, G. S. (1997). Some basic concepts of wave-particle
 514 interactions in collisionless plasmas. *Reviews of Geophysics*, 35(4):491–501.
- 515 Turner, D., Claudepierre, S., Fennell, J., O'Brien, T., Blake, J., Lemon, C.,
 516 Gkioulidou, M., Takahashi, K., Reeves, G., Thaller, S., et al. (2015). Energetic
 517 electron injections deep into the inner magnetosphere associated with substorm
 518 activity. *Geophysical Research Letters*, 42(7):2079–2087.
- 519 Ukhorskiy, A. Y., Anderson, B. J., Brandt, P. C., and Tsyganenko, N. A. (2006).
 520 Storm time evolution of the outer radiation belt: Transport and losses. *Journal of
 521 Geophysical Research: Space Physics*, 111(A11):n/a–n/a. A11S03.
- 522 Van Allen, J. A. (1959). The geomagnetically trapped corpuscular radiation. *Journal
 523 of Geophysical Research*, 64(11):1683–1689.
- 524 Vernov, S. and Chudakov, A. (1960). Investigation of radiation in outer space. In
 525 *International Cosmic Ray Conference*, volume 3, page 19.

- 526 Woodger, L., Halford, A., Millan, R., McCarthy, M., Smith, D., Bowers, G., Sample,
527 J., Anderson, B., and Liang, X. (2015). A summary of the BARREL campaigns:
528 Technique for studying electron precipitation. *Journal of Geophysical Research: Space Physics*, 120(6):4922–4935.
529